

Orographic Precipitation in Coastal Southern Chile: Mean Distribution, Temporal Variability, and Linear Contribution

R. GARREAUD

Department of Geophysics, and Center for Climate and Resilience Research, Universidad de Chile, Santiago, Chile

M. FALVEY

Department of Geophysics, Universidad de Chile, Santiago, Chile

A. MONTECINOS

Department of Geophysics, and Centro de Recursos Hídricos para la Agricultura y Minería, Universidad de Concepción, Concepción, Chile

(Manuscript received 16 September 2015, in final form 31 December 2015)

ABSTRACT

The Nahuelbuta Mountains (NM) are a semielliptical massif 1300 m high in coastal southern Chile (37°–38°S) facing frontal storms that move from the Pacific. Mean precipitation between 900 and 1200 mm yr⁻¹ is observed in the surrounding lowland, but river flow measurements suggest values ≥ 3000 mm yr⁻¹ atop the mountains. To verify and characterize such marked orographic enhancement, 15 rain gauges were deployed around and over the NM. The observations were supplemented by a high-resolution WRF simulation and linear theory (LT) modeling during the winter of 2011. The estimated mean precipitation increases gradually from offshore (~ 1000 mm yr⁻¹) to the north-facing foothills (2000 mm yr⁻¹). The precipitation rapidly increases in the upslope sector to reach ~ 4000 mm yr⁻¹ over the northern half of the NM elevated plateau, and decreases farther south to reach background values 20–30 km downstream of the mountains. The upstream (downstream) orographic enhancement (suppression) was relatively uniform among storms when considering event accumulations but varied substantially within each storm, with larger modifications during pre- and postfrontal stages and minor modifications during the brief but intense frontal passage. WRF results are in good agreement with observations in terms of seasonal and daily mean rainfall distributions, as well as temporal variability. Given its linear, steady-state formulation, the LT model cannot resolve rainfall variability at short (hourly) time scales, which in WRF is at least characterized by transient, mesoscale rainbands. Nonetheless, the rainbands are mobile so the accumulation field at monthly or longer time scales produced by the linear model is remarkably similar to its WRF counterpart.

1. Introduction

Precipitation enhancement over the windward slopes of major mountains and a rain shadow in their lee is a very familiar pattern in hydrometeorology resulting from seemingly simple dynamics: forced ascent of moisture-laden air parcels upstream of the mountain and downstream subsidence. Quantifying precipitation

over mountainous terrain, however, remains challenging (because of its scale dependence and the complex interrelation between airflow dynamics and cloud microphysics) and follows three main approaches. First, gridded precipitation products can be obtained by ingesting in situ records or remotely sensed data into geostatistical methods with varying degrees of sophistication (Hevesi et al. 1992; Basist et al. 1994; Daly et al. 1994, 1997; Frei and Schär 1998; Prudhomme and Reed 1998, 1999). The nature of mountainous terrain—rugged and often inaccessible—goes along with a low density of surface stations and blocking of radar beams, limiting the application of this method. Second, full-physics,

Corresponding author address: Dr. René Garreaud, Department of Geophysics, Universidad de Chile, Blanco Encalada 2002, Santiago 2777, Chile.
E-mail: rgarreau@dgf.uchile.cl

three-dimensional numerical models of the atmosphere are now widely used to produce weather forecasts, reanalysis of past events, and simulations of idealized cases of orographic precipitation (e.g., [Alpert and Shafir 1989](#); [Barros and Lettenmaier 1993](#); [Sinclair 1994](#); [Colle 2004, 2008](#)). When integrated with a high resolution (horizontal grid spacing ≤ 5 km), the models become computationally expensive thus limiting the possibility of long-term simulations, ensemble runs, and sensitivity studies.

A third approach to orographic precipitation considers the use of simpler, quasi-analytical models linking water vapor flux and orographic precipitation ([Barros and Lettenmaier 1994](#); [Smith 2003](#); [Barstad and Smith 2005](#); [Kunz and Kottmeier 2006a](#)). The precipitation pattern in a quasi-analytical model can be diagnosed on the basis of a few physical parameters (e.g., the time scale of autoconversion) and environmental conditions (e.g., incoming wind speed). Furthermore, because these are fast-solving models, they are attractive for coupling with landscape and geomorphology models (e.g., [Roe et al. 2003](#); [Anders et al. 2007, 2008](#)) to produce long-term simulations. These models are based on a number of premises that generally restrict their use to the linear regime [[Barstad and Smith \(2005\)](#), their Table 2], and yet they produce climatological (long-term mean) mountain precipitation patterns in good agreement with observations. Realistic precipitation climatologies based on linear models include Oregon's climate transition ([Smith et al. 2005](#)) and the Olympic Mountains ([Anders et al. 2007](#)) in western North America, as well as in the Black Forest Mountains in Germany ([Kunz and Kottmeier 2006b](#)) and the southern Andes ([Smith and Evans 2007](#)). Given prescribed environmental conditions (e.g., wind and temperature profiles), the linear models resolve the steady-state precipitation field. In the real world, the environmental conditions are continuously varying in time (and space), but in practice the forcing of a linear model is updated at a finite time interval (e.g., by using radiosonde information every 12 h). Therefore, down to which temporal scales the application of a linear model produces a realistic simulation of orographic precipitation is still an open question.

In this work, we study the orographic precipitation over the Nahuelbuta Mountains (NM) in coastal southern Chile (38°S) where precipitation is largely produced by the passage of frontal systems embedded in midlatitude cyclones. To this end, we use an enhanced network of surface observations, a full-physics simulation using the Weather Research and Forecasting (WRF) Model, and results from a linear theory (LT) model developed by [Smith and Barstad \(2004\)](#). Details on the observations and models are provided in [section 2](#). A geographical background and meteorological

context is provided in [section 3](#) and [appendix A](#). A description of the orographic precipitation over the Nahuelbuta Mountains is presented in [section 4](#), including its seasonal mean distribution as well as inter- and intrastorm variability. In that section, we show that WRF results agree well with the observations from daily to seasonal time scales.

The observed and WRF-simulated orographic precipitations are further compared with the results from the linear model precipitation at different time scales, from hourly to seasonal. Deviation from linearity can arise from several reasons: the threshold character of the water vapor saturation (e.g., [Durrán and Klemp 1982](#)), inherent nonlinearity in various microphysical processes (e.g., collision-coalescence of rain droplets; see [Jiang and Smith 2003](#)), the full or partial blocking of the moist airflow by sharp topography ([Jiang 2003](#)), and the release of convection within orographic clouds if the incoming air is potentially unstable (e.g., [Kirshbaum and Durrán 2005](#); [Kirshbaum et al. 2007](#)). Although we have not explicitly analyzed the source of these nonlinear effects, the discrepancies between the LT model and WRF results are indicative of their incidence on orographic precipitation and discussed in [section 5](#). Concluding remarks are presented in [section 6](#).

2. Data and models

a. Observational data

Precipitation data in Chile are primarily supplied by the National Weather Service [Dirección Meteorológica de Chile (DMC)] and the National Water Authority [Dirección General de Aguas (DGA)], which operate networks of meteorological stations. While these sources are reliable and encompass several decades, most of the stations are conventional (reporting daily accumulations only) and located at low elevations. Therefore, to describe the precipitation distribution over NM, we installed and operated our own network of rain gauges from May 2011 to September 2013. The so-called Andes Frontal Experiment (AFEX) network was composed of 17 HOBO RG3 tipping-bucket rain gauges (registering 0.2-mm rainfall "events") and solar-shielded air thermometers installed at about 1 m above ground. All AFEX stations were located in clear, unobstructed areas. Details on the AFEX stations are presented in [Table 1](#). The original HOBO data were transformed into time series of 30-min rainfall accumulation and average air temperature. Our experience during field visits indicates that near-surface winds can exceed 10 m s^{-1} during some storms in stations located in the windward (northern) slope of NM. Calculating the undercatch of

TABLE 1. Name, code, and location of the AFEX stations (see Fig. 1). Their observing periods are also given.

Station name	Code	Lat (S)	Lon (W)	Elev (m MSL)	Observing period
Curanilahue	CUR	37.47°	73.34°	137	From June 2011 to September 2013
MEO-1	MEO	37.51°	73.31°	310	From May to September 2011
Torre Arauco 1	TNO	37.53°	73.26°	731	From May to September 2011
Torre Bomberos	TBO	37.56°	73.22°	994	From May 2011 to September 2012
Escuela Trongol Alto	ETA	37.56°	73.17°	750	From June 2011 to November 2013
Alto tres pinos	A3P	37.62°	73.11°	1044	From May to September 2011
Cerro Alto Arauco	CAR	37.70°	73.11°	1382	From May to September 2011
El Bajo	EBA	37.73°	73.05°	763	From May to November 2011
Fundo Santa Marta	FSM	37.68°	73.26°	195	From May to September 2011
Torre Caramavida Sur	CAS	37.72°	73.21°	1071	From May to September 2011
Torre Caramávida Norte	CAN	37.66°	73.29°	760	From May to September 2011
Parque Este	PQE	37.82°	72.96°	1177	From May to September 2011
Escuela Oscar Muñoz	EOM	37.75°	72.88°	907	From May to September 2011
Torre El Sauce	TES	37.92°	72.91°	862	From May to September 2011
San José Colico	ECO	37.36°	73.33°	130	From July 2011 to September 2013
Corriente Alto	COA	37.32°	73.11°	901	From May to September 2012
Isla Santa Maria	ISM	36.90°	73.52°	47	From April to November 2013

rainfall due to the airflow around the gauge would require local measurements of the wind speed (e.g., Yang et al. 1998; Sieck et al. 2007) that are not available during AFEX, but we present a rough estimate of the wind-induced negative bias in sections 4a and 4b.

The location of the AFEX stations is shown on the topographic map of Fig. 1b together with the location of the DMC/DGA rain gauges available for this study. The AFEX stations were preferentially installed along a northwest–southeast transect, coinciding with the prevailing

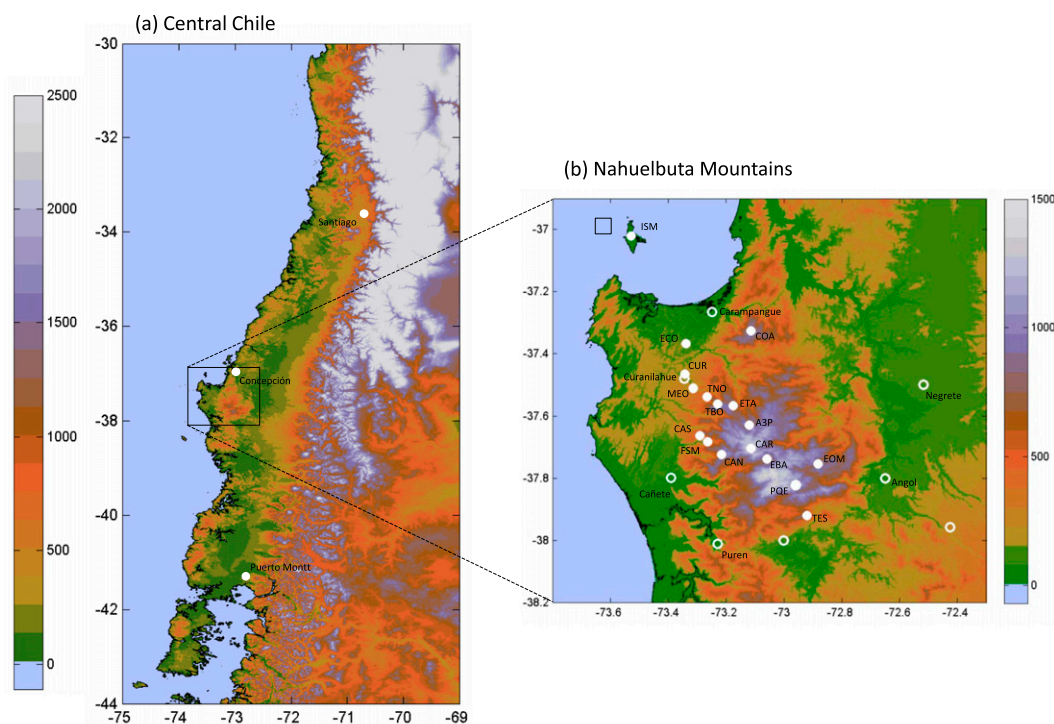


FIG. 1. Topographic maps of (a) south-central Chile and (b) NM area. In (b), filled circles correspond to the location of the AFEX rain gauges (see codes and further details in Table 1) and open circles correspond to the location of meteorological stations from DMC/DGA used in this study. Note that the color scale is different in each map. The small box in (b) near Isla Santa Maria indicates the column in WRF intermediate domain from where we take the wind and thermodynamical profiles to force the LT model.

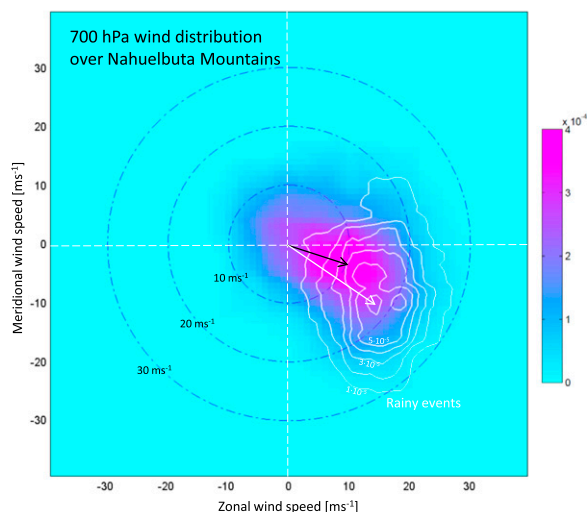


FIG. 2. Bidimensional histogram of the 700-hPa winds over the NM. The histogram was constructed using the zonal and meridional wind components every 3 h (from 1 May to 15 Sep 2011) from the WRF results for a grid box just off the coast (see Fig. 1b). The background colors indicate the wind distribution considering all temporal samples. The white contours indicate the wind distribution for rainy samples in CUR [$>1 \text{ mm (3 h)}^{-1}$]. The black and white arrows are the mean wind vectors for all samples and rainy samples in CUR, respectively.

wind direction during rainstorm events (e.g., Fig. 2) and thus recording rainfall in the upstream sector (two stations), foothill (two stations), windward slope (three stations), elevated plateau (three stations), and downstream of the NM (three stations). Only three AFEX stations were installed off the main transect, two of them to sample precipitation in a small catchment draining toward the west and one station on a nearby, isolated mountain.

b. WRF simulations

To supplement the observational results, we performed a high-resolution numerical simulation using the WRF Model (version 3.2; Skamarock et al. 2005). Parameterizations are listed in Table 2. Three nested domains were used in this simulation. Results presented here are taken from the inner domain with a horizontal grid spacing of 1 km and 44 σ levels, spanning a rectangular region (162×156 points) centered at the NM. An intermediate domain with 3-km horizontal resolution covers part of southern Chile and the adjacent ocean, while the mother domain with 9-km horizontal resolution spans the region 18° – 26° S, 77° – 66° W. A realistic topography was employed in each domain. Global Forecast System (GFS) analyses (0.5° latitude–longitude grid, every 6 h) were used as initial and boundary conditions for the mother domain.

TABLE 2. WRF parameterizations.

Parameterization	Reference
Thompson microphysics scheme	Thompson et al. (2004)
Longwave radiation: Rapid Radiative Transfer Model	Mlawer et al. (1997)
Shortwave radiation: Dudhia	Dudhia (1989)
Pleim–Xiu land surface model	Pleim and Xiu (2003)
Monin–Obukhov surface scheme	Janjić (2002)
Mellor–Yamada–Janjić boundary layer scheme	Janjić (2002)
Betts–Miller–Janjić cumulus scheme	Janjić (2000)

WRF was integrated continuously from 1 May to 15 September 2011, thus encompassing the whole austral winter and part of the spring when most of the AFEX satiations were active. Results were saved every 1 h and compared against observations whenever possible (sections 4b and 4c).

c. The LT model

To address the linearity of the orographic precipitation we used the LT model developed by Smith and Barstad (2004). This model computes the airflow over the topography using linear mountain wave theory. In doing so, it assumes steady-state, uniform horizontal wind and moist static stability across the domain, as well as upstream saturation. Under these conditions, ascent initiates formation of cloud water droplets that drift downstream while converting to hydrometeors on a time scale τ_c and fall to the ground on a time scale τ_f . Drying in areas of descent leads to subsaturated conditions and evaporation of hydrometeors. The linear airflow dynamics and cloud physics equations are jointly solved using a two-dimensional Fourier transform to obtain a single formula relating terrain and precipitation. Details of this formulation are presented in the original work by Smith and Barstad (2004), as well as in Smith (2006) and Smith et al. (2005).

Several parameters must be specified to run the LT model, including surface temperature, wind speed and direction, and the moist Brunt–Väisälä frequency. In our work, these parameters were obtained from the WRF intermediate domain (3-km resolution) considering the hourly outputs in a column just off the coast, near Isla Santa Maria (see Fig. 1b). Estimated values of the cloud delay times range between 200 and 2000 s (Jiang and Smith 2003; Smith et al. 2005) and may be adjusted to obtain the best match with observed precipitation patterns in each event (e.g., Barstad and Smith 2005). Here we simply set $\tau_c = \tau_f = 1000$ s following Smith and Barstad (2004) and the successful application of the LT model in the Olympic Mountains (somewhat similar to

the Nahuelbuta Mountains) by Anders et al. (2007). In section 5, we also briefly report results using other cloud delay times. Using this configuration, the linear model was applied in the same inner domain of WRF with a horizontal grid spacing of 1 km using elevation data from the Shuttle Radar Topography Mission (SRTM).

To obtain the accumulated precipitation from the instantaneous rainfall field provided by the LT model, we assumed invariant forcing within each hour. Regardless of the environmental conditions, the LT model generates orographic precipitation somewhere over the domain at every time step, leading to unrealistically high seasonal accumulations. In the real world, orographic precipitation in a midlatitude setting is rather episodic and occurs most often as an enhancement of a large-scale precipitating system (e.g., Smith 2006). Here, we added the hourly LT model orographic precipitation only when the forcing wind was from the western or northern quadrants (wind direction from 225° to 45°) and the relative humidity exceeded 85% between 500 and 1500 m MSL at a coastal point upstream of NM. Such empirical rule was based on the synoptic examination of rainfall events over the NM (appendix A) and resulted in the exclusion of 93% of the hourly cases with LT model precipitation (somewhere in the mountains) without observational or WRF counterparts. The exclusion fraction does not change much (89%–94%) when varying the relative humidity threshold between 80% and 95%. Even with this rule, 37% of the total hourly rainfall “snapshots” simulated by the LT model were aggregated into the seasonal (the winter of 2011) accumulation.

3. Geographical setting and meteorological background

The west coast of South America is characterized by its prominent topography (Fig. 1a). To the south of 33°S there is a well-defined coastal range that in many places rises over 1000 m MSL, an elongated central valley at an average elevation of 500 m, and the Andes cordillera that rises sharply to its top within 200 km from the coastline. The height of the Andes decreases southward from more than 5000 m MSL at subtropical latitudes to about 1500 m MSL at 40°S.

The NM dominates the coastal range between 37° and 38°S (Fig. 1b). The massif has a semielliptical shape about 150 km long and 100 km wide, reaches 1300 m MSL, and presents an extensive area between 1000 and 1200 m that we refer as to the elevated plateau. The cool, humid climate of NM provides favorable conditions for Araucaria forests, other indigenous plant species, and some rare mammals only found in the more remote

Andes cordillera or several hundred kilometers farther south (e.g., Endlicher and Mäkel 1985; Donoso et al. 2008). Given its ecological relevance, the southern half of the elevated plateau has the status of a national park.

Coastal and low-elevation inland sectors surrounding the NM receive about 1000 mm yr⁻¹ of precipitation. By using a water balance and the streamflow measurements in rivers that drain the NM, however, values in excess of 3000 mm yr⁻¹ have been estimated atop the mountains (DGA 1987), indicative of a marked precipitation enhancement in the mountains. Precipitation in south-central Chile is largely associated with the passage of cold fronts (Falvey and Garreaud 2007) and therefore is concentrated from late fall to early spring (May–September; Viale and Garreaud 2015). Given their synoptic nature, rainstorms over the NM typically last 1–2 days and have a quasi-weekly recurrence. During the winter of 2011 (our main observing period), 28 storms affected the region, and a cold front (as per the wind shift and air temperature drop) was identified in all but three cases. The onset (demise) of each individual storm corresponds to the first (last) time in which continuous precipitation (for the next/past 12 h) was observed in either of the two stations in the NM foothills (CUR and MEO-1; see Table 1 for a list of station names and codes). Some regional-scale features of a cold front passage over the NM are illustrated for a typical case in appendix A. The three nonfrontal cases were associated with so-called warm storms (Garreaud 2013) with persistent warm, westerly flow.

In any case (cold fronts or warm storms), analysis of WRF-simulated thermodynamics profiles upstream of NM hardly reveals little, if any, conditional instability. We searched for conditionally unstable layers (defined here as a layer of at least 250 m deep with a simulated lapse rate between saturated adiabatic lapse rate and dry adiabatic lapse rate) and found they occurred less than 8% of the time when rainfall was observed over the NM foothills (>0.5 mm in CUR or MEO-1 stations). In a more recent field campaign [Chilean Coastal Orographic Precipitation Experiment (CCOPE-2015; J. Minder et al. 2015, poster presentation)] 25 radiosondes were launched about 40 km upstream of the NM foothills during winter storms and a conditionally unstable profile occurred in only four cases (even in those cases, surface-based CAPE values were less than 50 J kg⁻¹). Therefore, both WRF simulations during AFEX and CCOPE-2015 soundings suggest that stable, stratiform precipitation is by far the predominant type of winter storm in the NM. Nonetheless, this does not preclude the occurrence of embedded convection in stratiform precipitation, especially during the post-frontal conditions, as described by Fuhrer and Schär

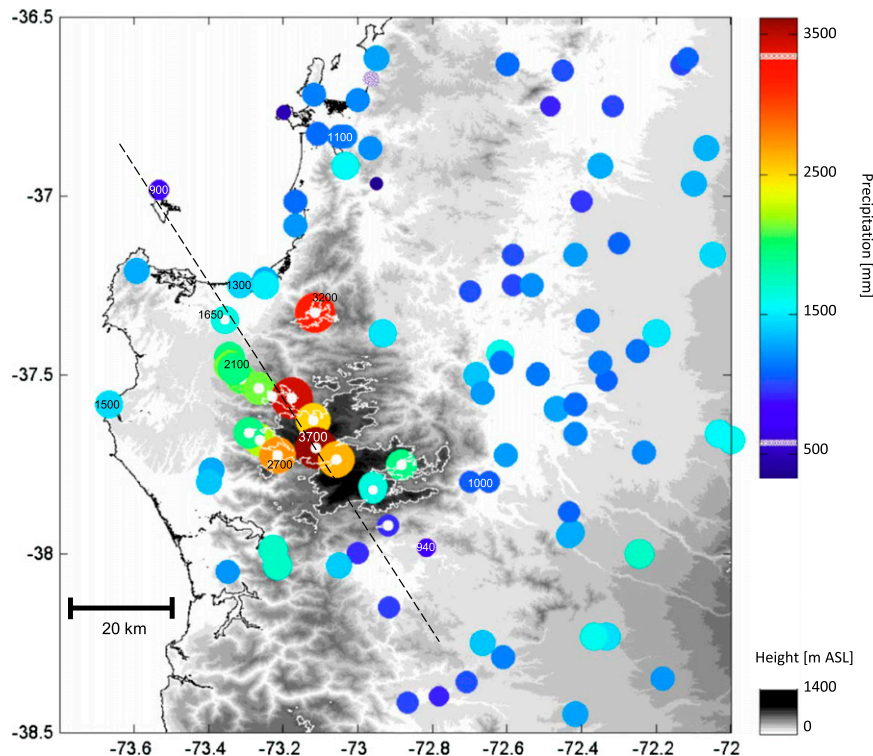


FIG. 3. Estimated annual mean precipitation over the NM and surrounding areas based on station data (see details in [appendix A](#)). The circles are color coded according to the annual mean precipitation and superimposed on a topographic map. A few values are indicated for reference. Circles with a white dot inside are the AFEX rain gauges; others are regular DMC/DGA stations.

(2005) and [Kirshbaum et al. \(2007\)](#). Unfortunately, the absence of radar data during AFEX or CCOPE-2015 hinders identification of convective cells or their contribution to the winter precipitation over NM.

The free-tropospheric wind over NM during rainfall periods is almost exclusively from the northwest quadrant, as shown by the bidimensional histogram of the WRF-simulated wind components at the 700-hPa level ([Fig. 2](#)) in a column about 50 km to the northwest of the mountain top (indicated in [Fig. 1b](#)) with a mean speed of 20 m s^{-1} . Northwesterly flow also prevails during rainfall episodes near crest level but with lower mean speed (15 m s^{-1} , not shown). When rainfall is not present, the average flow is weaker and more westerly, although wind direction has more spread, including periods with southerly winds. For each hour with rainfall over the NM foothills ($>0.5 \text{ mm}$ in CUR or MEO-1 station), we calculated the inverse Froude number $\varepsilon = N_m h_x / U$ where $h_x = 1250 \text{ m}$ is the mountain height, U is the upstream wind speed perpendicular to the mountain averaged between 200 and 1200 m MSL, and N_m is the moist Brunt–Väisälä frequency averaged in the same layer [the so-called averaging method by [Reinecke and Durran \(2008\)](#)]. Both U and N_m profiles were

obtained from a WRF column offshore of the Nahuelbuta sector. Linear theory predicts that windward stagnation occurs as ε approaches 1 ([Smith 1988, 1989](#)). The average value of ε when rainfall is present is ~ 0.67 with an interquartile range of 0.56–1.12. Therefore, most of the time the bulk of the incoming airflow can pass over the mountains when rainfall occurs, giving support to the use of a linear model for winter storms in the NM. Yet, windward flow deceleration and flow splitting occurs nearly 20% of the time. Using WRF results and surface observations, we also estimated the freezing level height when rainfall is present, resulting in a median value of 1230 m MSL with an interquartile range of 950–1650 m MSL.

4. Orographic precipitation over the NM

a. Observed mean rainfall distribution

Here, we use the observations from the AFEX network to explore some features of the mean spatial distribution of precipitation over the NM. Since the AFEX data cover only a few years, we use concurrent records and long-term averages from nearby

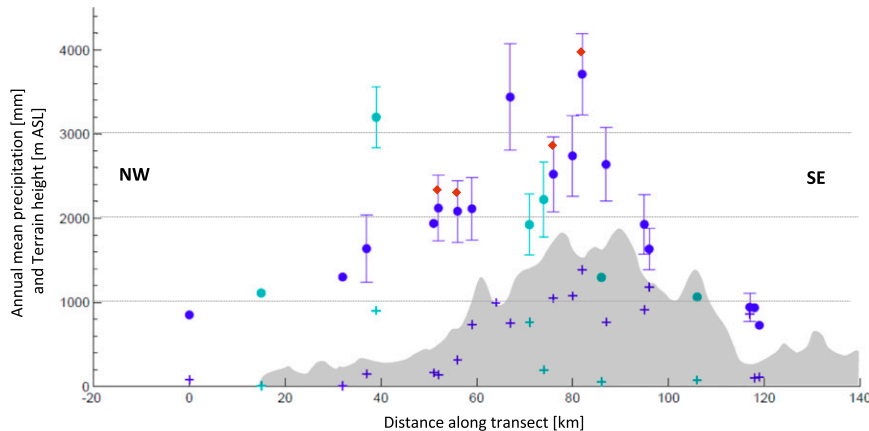


FIG. 4. Estimated annual rainfall (symbols) and topographic profile (area) along a northwest–southeast transect throughout the NM (see Fig. 3). Blue circles indicate precipitation in stations within 10 km of the transect. Green circles indicate precipitation in stations >10 km away from the transect. Circles with error bars are AFEX estimates; circles without error bars are regular DMC/DGA stations. The error bars are the standard deviation of the five estimates of the climatological accumulations described in appendix B. The red diamonds in four stations in the windward slope of the NM are an upper bound of the annual mean precipitation considering a 10% wind-induced undercatch. Crosses indicate the station height.

DMC/DGA stations to obtain estimates of the mean annual precipitation (MAP) over the mountains (see appendix B for details). Furthermore, because stations located on the windward (northern) slope of the NM can undercatch rainfall because of wind exposure [see reviews in Sieck et al. (2007); Adam and Lettenmaier (2003)], the values reported here may be up to 10% lower than the actual accumulation. The results are shown in Fig. 3, where the observed mean precipitation is superimposed on the topographic map, as well as in Fig. 4 by a transect that begins in Isla Santa Maria and continues through the mountain range with a northwest–southeast direction.

Moving southward along the transect, MAP increases from less than 1000 mm offshore to 1500 mm in the upstream lowland sector and reaches just over 2000 mm near the foothills (CUR station). The estimated MAP remains approximately uniform in the next three stations over the windward slope of the mountain even though their elevation ranges from 250 to 900 m MSL, probably because they are within 20 km in horizontal distance. Farther south, the stations over 1000 m MSL have MAP in excess of 3200 mm reaching a maximum of $3700 \pm 300 \text{ mm yr}^{-1}$ at Cerro Alto Arauco (our highest station, but not at the peak of the mountain range). Therefore, a mean annual precipitation of 4000 mm cannot be ruled out over the highest terrain, representing a fourfold (twofold) increase from the upstream coast (foothills) to the mountain top over a horizontal distance of about 80 km (40 km). Such climatological orographic

enhancement is within the range of the observations in other midlatitude mountains [Adam et al. (2006); see also reviews in Roe (2005); Smith (2006)].

One AFEX station located atop an isolated hill (700 m MSL) just downstream of the NM has a MAP of 900 mm that is similar to the values of two nearby lowland stations. This range of annual mean precipitation is only $\sim 10\%$ less than the values observed in the coastal zone upstream of NM. In contrast, the mean precipitation downstream of the Olympic Mountains—a coastal massif in western Washington, United States, not too different from the NM—is about 40% less than the coastal upstream values [e.g., Fig. 2 in Anders et al. (2007)]. The reason for the relatively minor and spatially confined rain shadow downstream of the NM deserves further study.

b. WRF mean rainfall distribution

Figure 5 shows the accumulated precipitation for the period May–September 2011 from the WRF simulation (inner domain, 1-km resolution). The model captures the general mean precipitation pattern described before with a gradual increase from the coast to the foothills, a marked increase over the elevated plateau, and a rapid decrease over the leeside down to background values. While WRF accumulates $\sim 50\%$ more precipitation than observed, such overestimation is rather uniform across the domain with little altitudinal dependence (Fig. 6). The model overestimation is slightly reduced when considering a 10% rainfall undercatch in

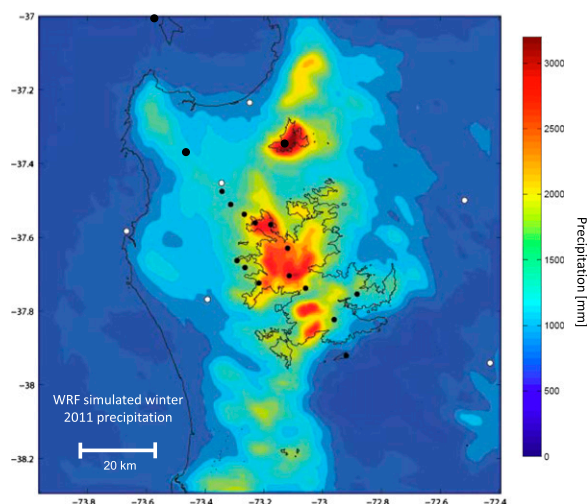


FIG. 5. Accumulated precipitation for the winter of 2011 (from 1 May to 15 Sep) simulated by WRF (results from the inner domain). The coastline and the 1000 m MSL topographic contour are indicated by black lines. Also shown are the location of the AFEX stations (black dots) and selected DMC/DGA stations (white dots).

the stations over the windward slope of the NM (red symbols in Fig. 6). Such percentage is an upper bound for the wind-induced bias in measured liquid precipitation (e.g., Sieck et al. 2007).

The seasonal mean WRF accumulation exhibits some features that supplement our observations. First, the highest accumulations (>3000 mm) are largely confined to elevations over 1000 m MSL (shown by the solid line in Fig. 5) within the northern (upstream) half of the elevated plateau, in contrast with the southern (downstream) half where precipitation is generally below 2000 mm. This variation across the plateau breaks down the generally tight relation between precipitation and altitude over the NM. Second, the mean precipitation field exhibits spatial heterogeneity tied to subrange topographic features with length scales as small as 20 km. For instance, precipitation along a transect that is oblique to the prevailing NW flow shows a decrease of 20% along a deep, narrow valley (10 km wide) relative to the values in the surrounding ridges (not shown). This WRF result is supported by the two AFEX observations in that transect. The sensitivity of the mean precipitation to small-scale topography over NM likely occurs during periods of shallow, warm precipitation, as it has been found elsewhere (Cosma et al. 2002; Minder et al. 2008). Finally, the WRF-simulated seasonal precipitation confirm that, at least for the winter of 2011, the NM rain shadow is confined (within 30 km downstream of NM) and rather minor (rainfall reduction $<15\%$ of the coastal upstream values).

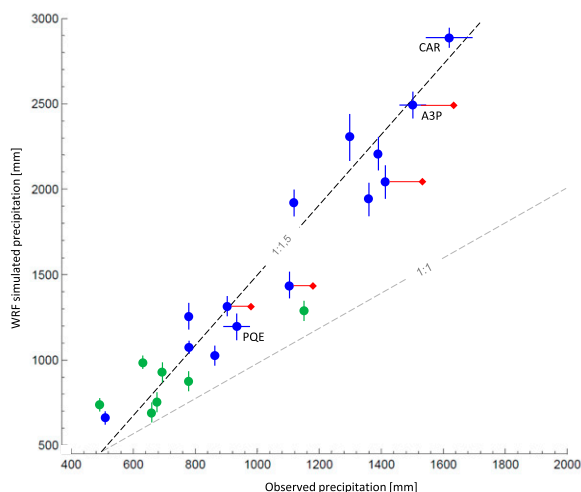


FIG. 6. Scatterplot of observed (x axis) and WRF-simulated (inner domain, y axis) accumulated precipitation for the winter of 2011 on the AFEX rain gauges (blue circles) and DMC/DGA stations (green circles). The WRF values are obtained by bilinear interpolation of the gridded results to the station location (latitude–longitude). The vertical lines indicate the standard deviation of the WRF results when offsetting such location by $\pm 0.1^\circ$ (~ 10 km). The horizontal lines in the three AFEX stations above 1100 m MSL (A3P, PQE, and CAR) are because the full winter precipitation was estimated there on the basis of the rain events only (see appendix B). The red diamonds in four stations in the windward slope of the NM are an upper bound of the observed precipitation considering a 10% wind-induced undercatch. The 1:1 and 1:1.5 lines are shown for reference.

c. Interstorm variability

A rough estimate of the upslope rainfall enhancement is provided by the ratio R_{upslope} of the accumulated precipitation over the northern edge of the elevated plateau (stations ETA and A3P) to the accumulated precipitation at the NM foothills (stations CUR and MEO-1). When considering the seasonal accumulation, $R_{\text{upslope}} = 2.1$, but the ratio varies between 1.3 and 3.2 for individual events (blue symbols in Fig. 7), excluding the three nonfrontal cases. The range of R_{upslope} expands significantly (from 0.8 to 4.9) using 3-h values when rainfall is present at the foothills. The ratio tends to be higher in those storms with larger accumulations at the foothills and stronger northwest low-level flow (not shown), as expected from a theory of orographic precipitation (e.g., Smith and Barstad 2004; Kunz and Kottmeier 2006a). Nevertheless, the correlation between R_{upslope} and northwest low-level wind (average between 100 and 1500 m MSL in the grid box shown in Fig. 1b) is 0.42 when considering storm averages and 0.31 when considering 3-h averages. A plausible explanation for these rather low values is that R_{upslope} considers the full precipitation field composed of both the

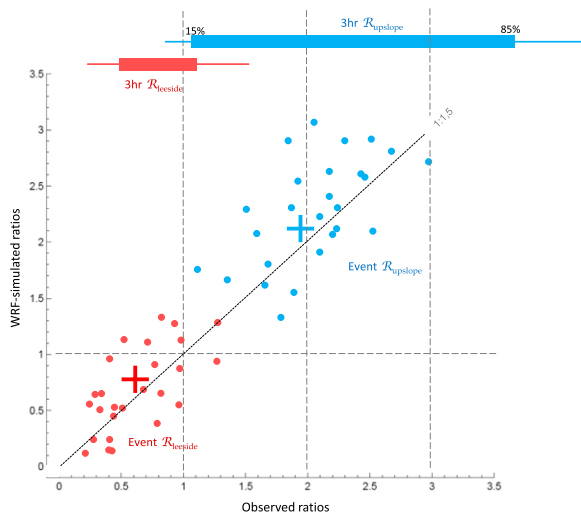


FIG. 7. Scatterplot of the observed (x axis) and WRF-simulated (inner domain, y axis) orographic modification ratios for the 26 frontal storms that crossed over the NM during the winter of 2011. The blue circles are the ratio between the storm-accumulated rainfall in upslope stations (average of ETA and A3P values) to the storm-accumulated rainfall in foothills stations (average of MEO and CUR values). The red circles are the ratio between the storm-accumulated rainfall in downslope stations (average of TES and EOM values) to the storm-accumulated rainfall in foothills stations. The thick crosses indicate the seasonal mean of both ratios. Also shown at the top of the figure are the range and 15% and 85% percentiles of the upslope and downslope orographic ratios constructed using observed 3-h rainfall accumulations at the corresponding stations.

orographic component as well as the large-scale precipitation that is independent of the topography. The breakdown of the linear relationship between upslope rainfall enhancement and wind as one considers shorter time scales is consistent with the results from Browning et al. (1974).

Likewise, the ratio of the accumulated precipitation on the stations downstream from the plateau (TES and EOM) to the accumulated precipitation at the NM foothills R_{leside} gives an estimate of the local rain-shadow effect (red symbols in Fig. 7). When considering seasonal accumulation, $R_{\text{leside}} = 0.6$, but the ratio ranges from 0.2 to 0.8 in individual storms and from 0.1 to 1.4 using 3-h values. While the strength of the leeside effect is variable and loosely dependent on the total precipitation and low-level winds, we note that $R_{\text{leside}} < 1$ (i.e., rainfall suppression) occurs in all events and $\sim 90\%$ of the 3-h samples.

Figure 7 also shows the ratios simulated by WRF for each storm using the grid points closest to the relevant AFEX stations. There is a good agreement between the observed and simulated storm ratios both in the upslope ($r = 0.76$) and leeside ($r = 0.61$), lending credibility to

the use of the WRF precipitation field as a complement to the AFEX observations.

d. Intrastorm variability

As noted before, the distribution of R_{upslope} and R_{leside} expands as one moves from events (typically about a day) to 3-h periods, reflecting a more variable orographic enhancement (or suppression) at shorter time scales. Indeed, the effect of the topography on the rainfall distribution varies substantially during the storm life cycle that here we have divided in prefrontal, frontal, and postfrontal stages. Following the procedure described in appendix A, we identified the frontal passage considering the low-level air temperature drop and the maximum rainfall rate at the NM foothills t_{max_p} for each of the 25 (out of 28) storms during the winter of 2011. The frontal stage was defined as the period of ± 1.5 h centered on t_{max_p} and the prefrontal (postfrontal) stage as the period with rainfall at the foothills before (after) $t_{\text{max}_p} - 1.5$ h ($t_{\text{max}_p} + 1.5$ h). Table 3 includes the multi-event mean ratios for each stage along with other selected statistics.

The average duration of the storms is ~ 30 h. The 3-h frontal stage has the highest rainfall rates, accounts for 20%–30% of the event accumulation (depending on the location), and exhibits the lowest orographic enhancement. On the other hand, the prefrontal stage is the longest (17-h average) and exhibits, on average, a five-fold foothill-to-mountain precipitation enhancement. In several cases, rainfall begins in the mountains up to 12 h before than at the upstream coastal sector. The foothill-to-mountain enhancement is also large (~ 5) during the postfrontal stage (10-h average), with many periods in which the decaying rainfall is restricted to the highest terrain.

Thus, the climatological foothill-to-mountain (coastal-to-mountain) rainfall enhancement ~ 2 (~ 4) obtained in section 4a results from quite variable conditions within individual storms (and to a lesser extent among different storms) from a minimum during the brief but intense frontal stage to a maximum during the prefrontal stage. Similar intrastorm variability is found for the downstream rainfall suppression (Table 3). Marked changes on the orographic precipitation during the storm evolution have also been documented in mountainous sectors of Great Britain (Browning et al. 1974, 1975), Germany (Egger and Hoinka 1992), and the western United States (Colle and Mass 1996; Lundquist et al. 2010).

5. Linear precipitation

In this section, we assess the contribution of linear processes to the total precipitation by comparing the

TABLE 3. Multievent statistics (mean \pm std dev) of the precipitation in the NM. Each of the 25 frontal storms was divided in a prefrontal, frontal, and postfrontal stage (see text for details). For each stage we calculated the mean duration (h); fraction of the total rainfall accumulation in foothill stations (CUR and MEO-1); rain rates at the foothill, windward slope (stations ETA and A3P), and leeside (stations TES and EOM); upslope rainfall enhancement (ratio of the accumulated precipitation in stations ETA and A3P to the accumulated precipitation in foothill stations), and leeside rainfall suppression [ratio of the accumulated precipitation on the stations downstream stations (TES and EOM) to the accumulated precipitation foothill stations].

Parameter	Prefrontal stage	Frontal stage	Postfrontal stage
Duration (h)	17 \pm 5	3	10 \pm 6
Foothill accumulation (%)	45 \pm 9	28 \pm 9	27 \pm 9
Foothill rain rate (mm h ⁻¹)	1.2 \pm 0.7	4.7 \pm 1	0.5 \pm 0.4
Mountain rain rate (mm h ⁻¹)	2.2 \pm 0.8	6.9 \pm 1.2	1.6 \pm 0.5
Leeside rain rate (mm h ⁻¹)	0.5 \pm 0.3	3.6 \pm 0.7	0.3 \pm 0.3
Upslope enhancement	5.1 \pm 0.4	1.4 \pm 0.5	5.5 \pm 0.9
Leeside suppression	0.3 \pm 0.2	0.8 \pm 0.5	0.5 \pm 0.3

rainfall distribution from the LT model to those from our AFEX observations and WRF simulation. Recall that the LT assumes that the flow over and around the mountain is linear (small departures from the mean flow) and uses a simplified, linear approach to the microphysical process (Smith and Barstad 2004). Figure 8a shows the accumulated orographic rainfall from the LT model for the winter of 2011 forced by WRF and limited to hourly periods with the proper environmental conditions for precipitation (see section 2c). To compare these results with those from WRF, we constructed a pseudo-orographic WRF rainfall (referred as to WRFO) for the winter of 2011 by subtracting the average precipitation in a box offshore, upstream of the mountains (representing the large-scale precipitation) to the precipitation in the rest of the grid boxes (Fig. 8b). This procedure is equivalent to add a background precipitation value to the LT model results and works well at monthly and longer time scales because the observed (or WRF simulated) accumulation field is rather uniform in the sector offshore of Nahuelbuta.

The similarity between the LT model and WRFO winter accumulation is evident, as both fields show the gradual enhancement upstream, a maximum over the elevated plateau, and a restricted rain shadow downstream. The WRFO accumulated precipitation, however, exhibits a sharper structure than its LT model counterpart. For instance, accumulations larger than 2500 mm are restricted to elevations above 1000 m MSL in WRFO, while in the LT model they also extend to the upslope. Moreover, compared with the WRFO results, the LT model winter accumulation is systematically higher (up to 500 mm) over the windward side of the NM, is lower over the leeward side, and exhibits a more extensive rain shadow.

These differences between the seasonal accumulation in LT model and WRF could be reduced by fine-tuning the cloud microphysics time scales used in the LT model

(e.g., Smith et al. 2005; Lundquist et al. 2010). We conducted two more simulations with $\tau_c = \tau_f = 500$ s and $\tau_c = \tau_f = 2000$ s. The first choice produced an accumulation too large atop the mountain (>5000 mm). In the second case, the maximum precipitation on top of NM is closer to its WRFO counterpart, but its spatial distribution is much smoother than observed. Thus, while not performing a full sensitivity analysis, our selection of $\tau_c = \tau_f = 1000$ s seems a reasonable choice for the purposes of this study.

We also note that the ratio of the mountain to coastal seasonal accumulation in the LT model (~ 7) is substantially larger than the observed and WRF-simulated ratios (~ 4). Indeed, the LT model produces relatively low accumulations in the lowland sectors 40–20 km upstream (to the north) of the NM foothills. A similar underestimation of the seasonal rainfall by the LT model upstream of the Southern California coastal ridge and northern Sierra Nevada has been reported by Hughes et al. (2009) and Lundquist et al. (2010), respectively. In both studies, the authors show that the LT model departs from the actual rainfall distribution during periods of low Froude number because nonlinear blocking leads to more ascent upwind of the mountains and more precipitation over the lower terrain. In the case of the NM, the incoming flow tends to be blocked in nearly 20% of the time (section 3), explaining, at least partially, the underestimation of the coastal/lowland precipitation relative to the values over the high terrain.

The spatial correlation between the WRFO and LT model winter accumulations reaches 0.87. Correlations above 0.7 are also obtained when considering monthly and even weekly accumulations, lending support to the use of a linear model to reproduce the mean distribution of orographic precipitation at seasonal or longer time scales. The spatial correlation,

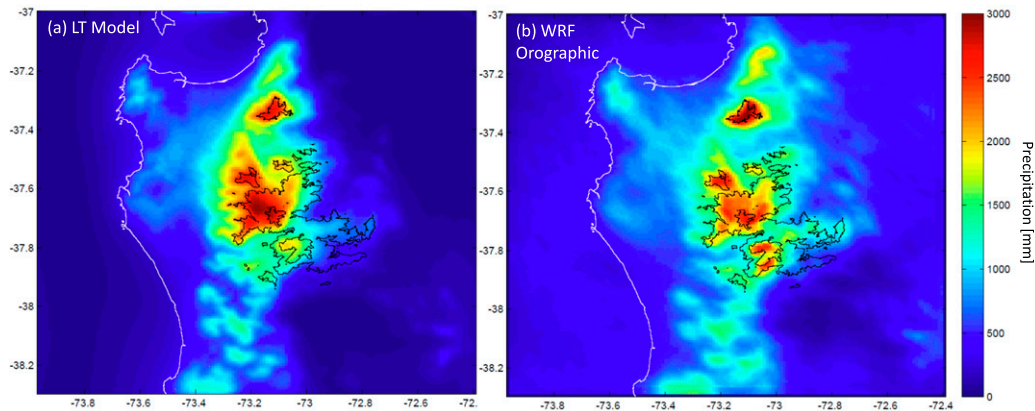


FIG. 8. (a) Accumulated orographic precipitation for the winter of 2011 simulated by the LT model (Smith and Barstad 2004). The coastline and the 1000 m MSL topographic contour are indicated by the white and black lines, respectively. (b) Accumulated orographic precipitation for the winter of 2011 simulated by WRF (results from the inner domain). The orographic precipitation was calculated by subtracting the hourly precipitation in a box offshore, upstream of the mountains (representing the large-scale precipitation) to the precipitation in the rest of the grid boxes.

however, reduces to less than 0.4 when considering daily accumulations because WRFO precipitation exhibits substantially more mesoscale structure than LT model results. To explore this issue in detail, we conducted special WRF simulations of one frontal case that occurred on 2 September 2011 (further described in appendix A). For the period from 1200 UTC 1 September to 1200 UTC 3 September, we run WRF with the same configuration than in our seasonal-long simulation (section 2b), and then run WRF with the terrain height set to zero in the inner domain (1-km resolution). Thus, a “true” WRF orographic precipitation can be obtained as the difference between the full-topography run minus the no-topography run. It is important to note that the pseudo-orographic precipitation used before is not applicable at subdaily time scales because a frontal passage produces much spatial variability across the whole domain so one cannot define a background precipitation (to subtract from WRF or add to the LT model).

Figure 9 shows hourly precipitation accumulation for both simulations at several stages during the frontal passage. The rather smooth LT model rainfall distribution contrasts with the richly textured true WRFO distribution, where banded, mesoscale structures are found during the whole storm and are especially prominent during the frontal stage. Consequently, the spatial correlation decays down to 0.2 (0.4) at hourly (3h) time scales (an hour is the minimum time interval to compare both simulations since the LT model is forced hourly). Intense rainfall rates ($>5 \text{ mm h}^{-1}$) can occur across

much of the domain (low and high terrain) in both the observations, WRF, and even WRFO, but are largely restricted to the elevated plateau in the LT model (not shown).

Determining the nature of these banded, mesoscale structures in WRF is beyond the scope of this work and requires a comprehensive observation system. One may speculate that small-scale topographic features may trigger convective orographic rainbands embedded in a stratiform orographic cloud when the moist incoming flow is weakly unstable (e.g., Kirshbaum and Durran 2004; Fuhrer and Schär 2005; Kirshbaum et al. 2007). Topographically induced horizontal wind shear in stable environments may also lead to localized enhanced precipitation (e.g., Houze and Medina 2005). The simulated rainbands, however, are not anchored over the topography, but they move with the mean low-level flow across the domain. More importantly, similar mesoscale structures appear in the no-topography WRF simulation (not shown), a strong indication that the simulated rainbands are inherent to the near-unstable environment during the frontal passage. Indeed, intense but narrow rainbands are well-known features in cold and warm frontal zones (e.g., Houze et al. 1976; Browning 1986; Matejka et al. 1980; Locatelli et al. 1995) even over open ocean. Although coastal mountains (as NM or the Olympic Mountains in western United States) can distort the frontal evolution in a variety of ways and locally enhance rainfall [see a review in Colle et al. (1999)], bands of intense precipitation may also occur in the absence of terrain effects, as also documented in Colle et al. (2002).

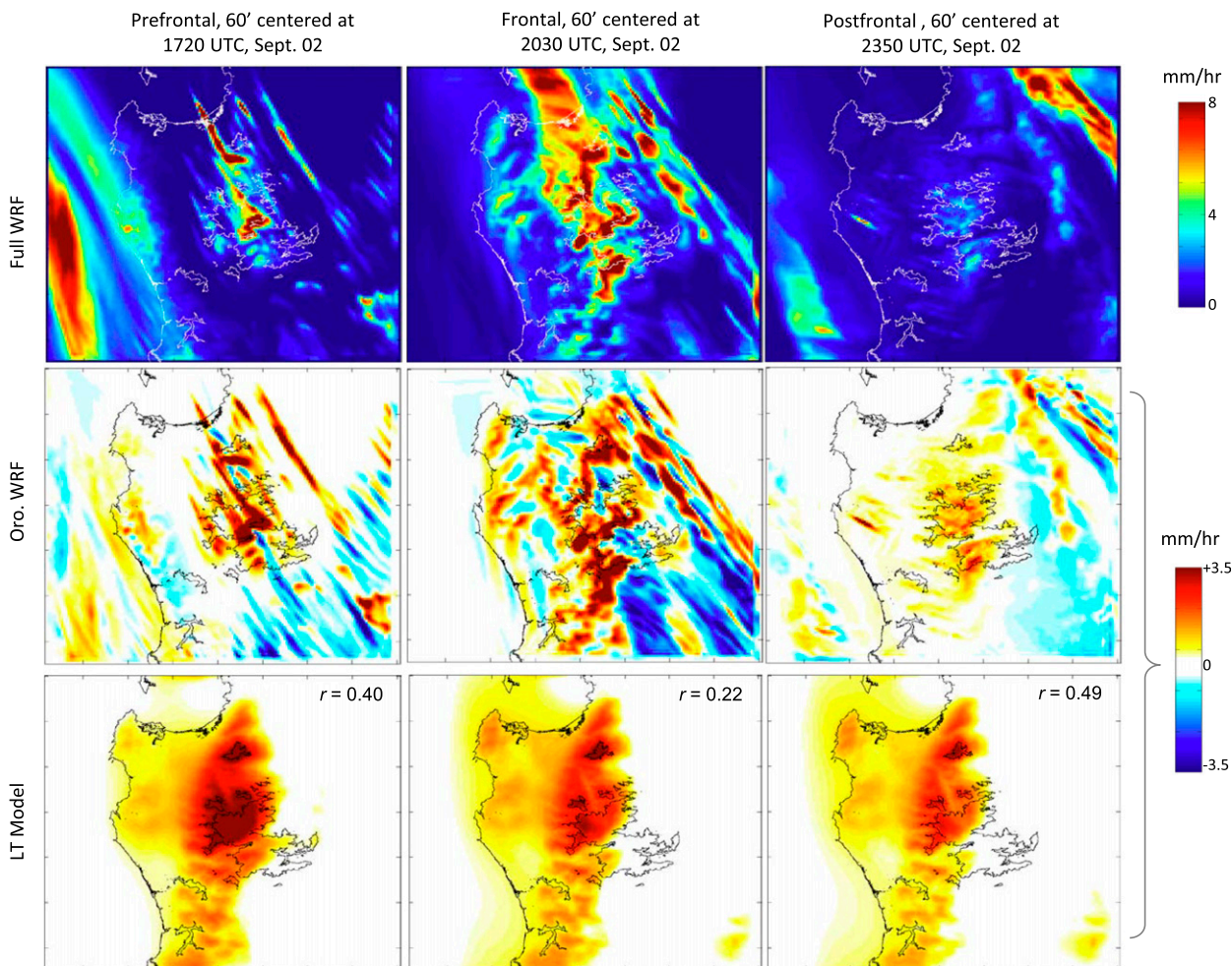


FIG. 9. Precipitation field during the passage of a frontal storm (2 Sep 2011) over the NM simulated by WRF and the LT model. Shown are hourly rain accumulations during (left) prefrontal, (center) frontal, and (right) postfrontal stages (time indicated above) for (top) WRF-simulated precipitation (inner domain), (middle) the “true” WRF orographic precipitation [calculated as the WRF full topography minus WRF no topography (see text)], and (bottom) the LT-model-simulated precipitation. The spatial correlation between the LT model precipitation and the WRF orographic precipitation is shown. The coastline and the 1000 m MSL topographic contour are indicated by thin lines.

So the question remains as to how two simulations (LT model and WRF) with such different rainfall distribution at subdaily time scales produce similar monthly and seasonal accumulations. While the WRF-simulated rainbands may be an actual ingredient of the near-instantaneous precipitation field, they are advected by the mean flow during the frontal passage, so their effect is smoothed at longer time scales.

The time series of rainfall offers another perspective on the extent to which the precipitation is linear. Let us consider the evolution of rainfall in the windward slope of the NM (station ETA) on 2 September 2011 (Fig. 10). Note that between 1200 and 1800 UTC, there is little or no precipitation in the observations but the LT model produces substantial precipitation. During this period,

however, the environmental conditions required to aggregate LT values (section 2c) are not yet present. The evolution of the linear model rainfall is smooth and continuous, in contrast with the WRF-simulated and observed time series that exhibit high-frequency variability. Specifically, after the frontal passage, the observed and WRF-simulated series exhibit periods with little or no precipitation alternating with periods of intense rain rates, perhaps reflecting the passage of the rainbands mentioned before. Also note that LT model orographic precipitation reaches its maximum a few hours before than in true WRF orographic precipitation, full WRF, and the observations. This is consistent with the occurrence of the strongest low-level winds just ahead of the frontal passage (appendix A).

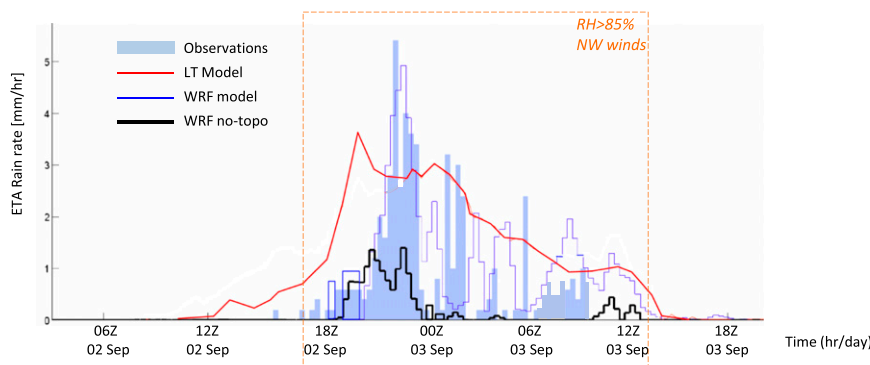


FIG. 10. Time series of rain rate at station ETA (in the windward slope of the NM) on 2 Sep 2011: observed (light blue bars), LT model simulated (red), WRF simulated (blue), and WRF no topography (black). The orange dashed box indicates the period when environmental conditions were proper to aggregate the LT model hourly data into the seasonal accumulation (see details in section 2c).

Figure 10 also reveals that the highest rainfall rates observed and those simulated by WRF are of comparable magnitude (up to 6 mm h^{-1}) and much higher than those in the LT model ($\sim 3 \text{ mm h}^{-1}$). This is expected since the observations and WRF include the large-scale component of the precipitation, but even if this component is added (for instance, adding the WRF no-topography values $\sim 1 \text{ mm h}^{-1}$), the LT model maxima are smaller than the observed and WRF-simulated rainfall maxima. These brief periods of intense precipitation are most likely related to localized convective circulations (either topographically forced or embedded in the frontal structure) or “seeder–feeder” type processes (e.g., Minder et al. 2008) that are not represented in the linear airflow, fixed microphysics formulation of the LT model.

The previous results are generalized in the scatterplot between the LT model and WRFO precipitation over the mountain box at event, daily, and 3-h time scales (Fig. 11). The temporal correlation of precipitation at a fixed point declines as one moves to shorter time scales (similar to what happens with the spatial correlation), and the LT model is not able to capture the short-lived (subdaily) periods of intense rainfall or the high-volatility present WRFO-simulated precipitation that also are evident in the observations.

6. Concluding remarks

The precipitation distribution over the Nahuelbuta Mountains in coastal southern Chile (38°S) has been documented using observations from a dedicated network of 17 rain gauges and conventional stations in the surrounding lowlands, complemented by results from a

continuous, high-resolution WRF simulation during the winter of 2011. Rainfall episodes (typically 1–2 days long) most often occur under moist northwest flow in connection with frontal passages. Our main results are as follows:

- The annual mean precipitation increases gradually from $\sim 1000 \text{ mm}$ in the coastal upstream zone to $\sim 2000 \text{ mm}$ over the foothills and windward slopes (50 km in the horizontal direction), and then more rapidly (about 25 km in the horizontal direction) to reach nearly 4000 mm over the northern half of the mountain’s elevated plateau ($\sim 1200 \text{ m MSL}$). Farther downstream, the precipitation rapidly approaches background values of $\sim 1000 \text{ mm}$. Thus, the NM generates a major upstream precipitation enhancement but a rather minor and spatially confined rain shadow downstream.
- Considering event accumulations, the orographic upstream enhancement (ratio of mountaintop to foothill values) varies from 1.3 to 3.2 (mean value of 2.1) and is only weakly related to the foothill precipitation and low-level northwest wind speed, most likely because the total precipitation is composed by the orographic component as well as the large-scale precipitation that is mostly independent of the topography.
- A much wider range of upstream enhancement is observed when considering shorter time scales (ratios from 0.8 to 4.9), from a minimum (~ 1) during the brief but intense frontal stage to a maximum (~ 5) during the longer pre- and postfrontal stages. In several cases, rainfall in the mountains begins (ends) up to 12 h before (after) the upstream coastal sector. Similar inter- and intrastorm variations are

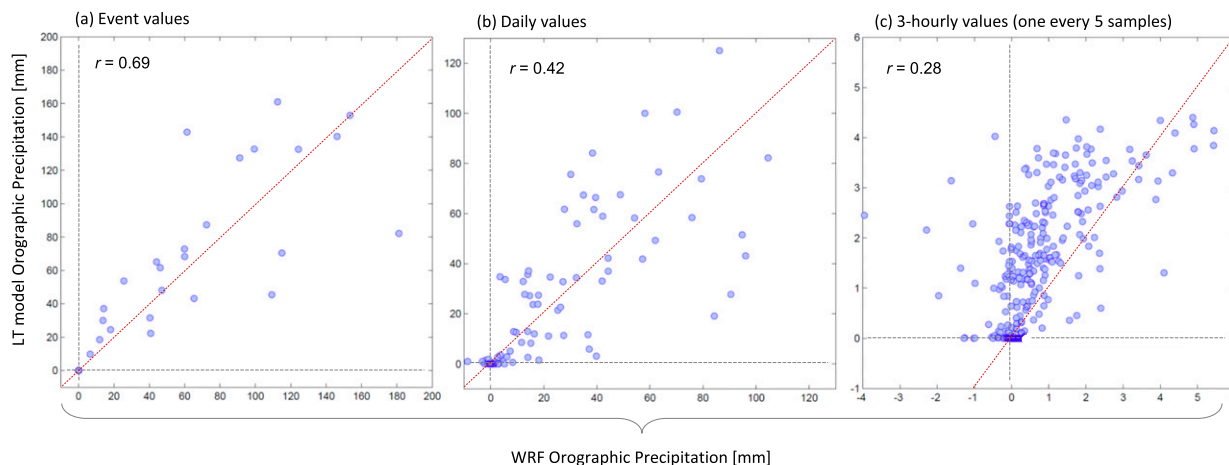


FIG. 11. Scatterplot between WRF-simulated orographic precipitation (x axis) and LT model precipitation (y axis) using (a) event, (b) daily, and (c) 3-h accumulations. The precipitation is evaluated in the grid box closest to ETA station (700 m MSL; upslope sector of the mountain).

found when considering the orographic downstream suppression.

- The WRF-simulated seasonal accumulation overestimates the observed values by a factor ~ 1.5 rather consistently across the domain. The model overestimation is slightly reduced when considering wind-induced rainfall undercatch (up to 10%) at stations over the windward slope of the NM. Otherwise, WRF results are in good agreement with the observations in terms of the spatial pattern, orographic modification ratios, and temporal variability. Of particular relevance, WRF was able to capture brief periods (1–3 h) with high precipitation rates that can occur over the mountains as well as over the upstream lowlands.

A linear model of orographic precipitation (LT model) was also run, forced every hour by WRF-simulated wind and thermodynamic profiles in an upstream column. The LT assumes that the flow over and around the mountain is linear (small departures from the mean flow) and uses a simplified, linear approach to the microphysical process (Smith and Barstad 2004). At daily and shorter time scales, the linear rainfall distribution is substantially different from its WRF counterpart, as the latter contains transient, mesoscale rainbands that are not presented in the smooth LT model results. The rainbands may be originated by nonlinear topographic effects (localized convection and blocking) or be inherent to the frontal environment (as suggested by their existence in no-topography WRF runs). Furthermore, time series of observed and WRF-simulated rainfall during winter storms are much more

variable than LT model time series and include brief periods (1–3 h) of intense rainfall that can occur almost everywhere across the domain but preferentially over the mountains. These brief, intense showers may trigger landslides (eventually shaping the landscape) and other hydrometeorological hazards and may be linked to the mesoscale rainbands. The rainbands, however, are not anchored to the topography, and thus their effect smooths out at monthly or longer time scales, so the accumulation field produced by a simple, fast-running linear model is remarkably similar to the result based on a more complex, computationally expensive full-physics meteorological model.

Acknowledgments. We are greatly thankful to Dr. R. B. Smith and I. Barstad for providing the computational code of their LT model. R.G. was supported by CR2/FONDAP-15110009, FONDECYT-1110169, and FONDECYT-1140637. A.M. was partially supported by CHRIAM/CONICYT/FONDAP-15130015. We thank the constructive criticism of three anonymous reviewers.

APPENDIX A

Frontal Features over Nahuelbuta Mountains

Some regional-scale features of a cold front passage over the NM are illustrated for a typical case on 2 September 2011 using WRF outputs from the inner domain (Fig. A1). Before landfalling, a band of maximum precipitation at the surface is located just behind the cold

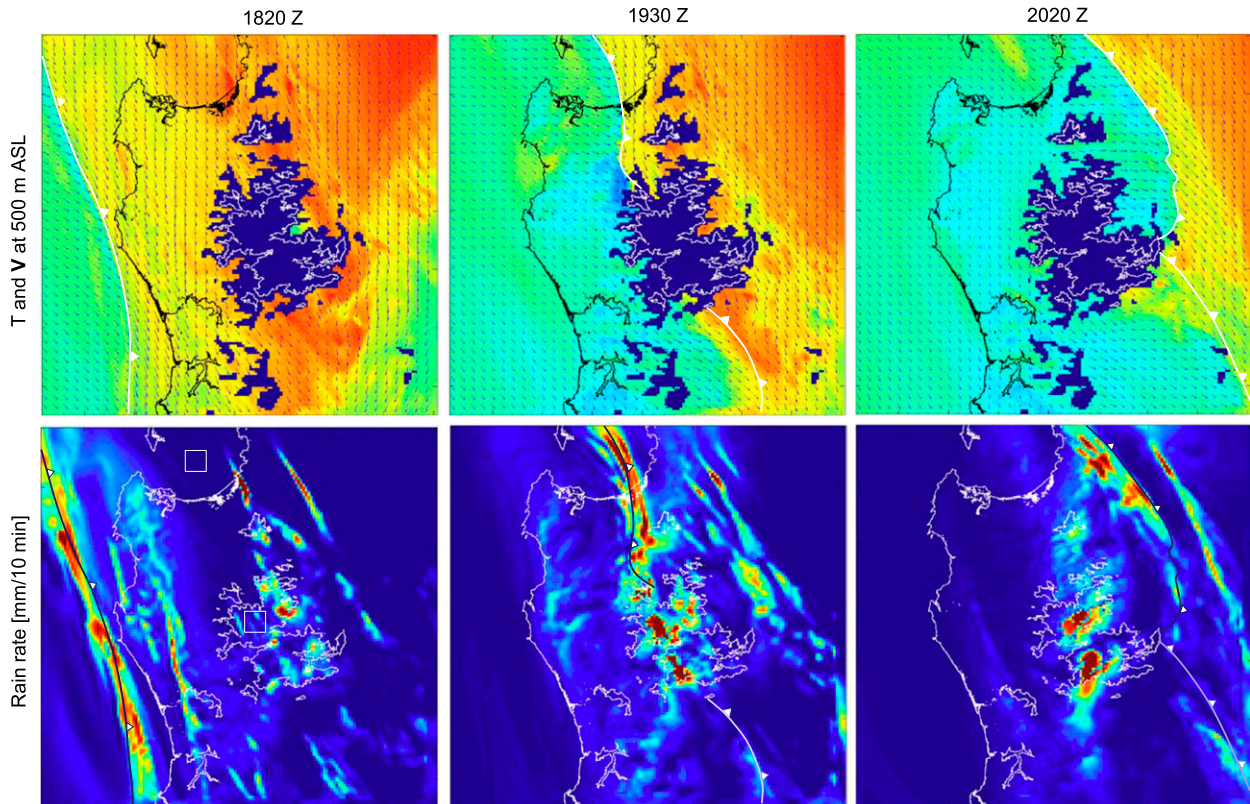


FIG. A1. Example of a frontal passage over the NM simulated by WRF (results from the inner domain, 1-km horizontal grid spacing, details in section 2b). The front crossed the area during the afternoon of 2 Sep 2011, and here we present snapshots at 1820 UTC (prefrontal), 1930 UTC (frontal), and 2020 UTC (postfrontal). (top) Air temperature and wind vectors at 300 m MSL; (bottom) rain rate at the surface (10-min rainfall accumulation centered in the time of each frame). The front is identified with conventional symbols; white line is the 700 m MSL topographic contour.

front, which in turn is readily identifiable by the wind shift. Transient, mesoscale areas of prefrontal precipitation are scattered across the domain, but they tend to be more persistent over the windward slope of the NM. Consistent with the rather small size of the massif, the surface front (as per wind shift and temperature gradient) maintains a high degree of coherence as it moves over and beyond the mountainous terrain. We also note that postfrontal precipitation is largely confined to the NM.

Twenty-eight storms were identified during the winter of 2011, and a cold front was identified in all but three cases in which warm, westerly flow prevailed [the so-called warm storms identified in Garreaud (2013)]. The frontal storms show fairly common features captured in a composite analysis of selected variables relative to the time of maximum precipitation $t_{\max p}$ at the foothills (Figs. A2, A3). The rainfall itself is relatively symmetric with respect to $t_{\max p}$, with slightly larger accumulation before than after the rainfall peak. The air temperature at the foothills exhibits a

weak increase until $t_{\max p}$ plus a few hours followed by a gentle decrease [$\sim 1^{\circ}\text{C} (12\text{ h})^{-1}$]. Farther up over the mountains the drop in air temperature is sharper [$\sim 3^{\circ}\text{C} (3\text{ h})^{-1}$], and within $\pm 1\text{ h}$ of $t_{\max p}$ it is indicative that the timing of precipitation maximum tends to coincide with the frontal passage. The significant rainfall accumulations during the prefrontal period (36–12 h before $t_{\max p}$) in the mountain stations are absent in stations away from the mountains (not shown) or in the composite analysis for rainstorms in central Chile (Garreaud 2013), revealing the role of the orography in the early onset (and hence longer duration) of rainfall over the mountains.

The free-tropospheric wind over NM during rainfall periods is almost exclusively from the northwest quadrant, as shown by the bidimensional histogram of the WRF-derived wind components at the 700-hPa level (Fig. 2). Consistent with the approach of a surface cold front and a trough axis aloft, the northerly component intensifies before $t_{\max p}$ throughout the tropospheric column (Fig. A3). Notably, the strongest low-level winds

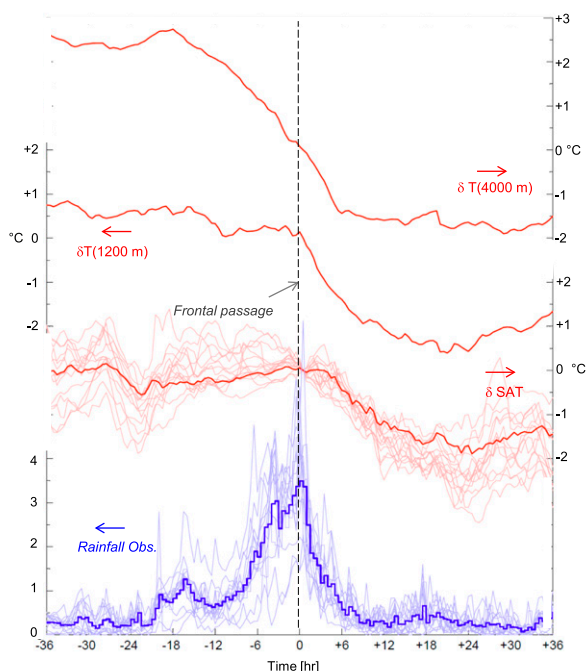


FIG. A2. Compositing analysis of selected variables during frontal passages over the NM. For each of the 26 frontal storms during the winter of 2011, we identified the time of maximum precipitation in station CUR at the mountain foothills, which is used as $t = 0$ for the compositing analysis. (from bottom to top) The thick blue line is the average rainfall for the 26 storms (individual cases in thin blue lines) using station data. The thick red line is the average temperature change (relative to $t = 0$) in CUR (thin lines are the individual cases) using station data. The next red line is the average free-tropospheric temperature change (relative to $t = 0$) over CUR at 1200 m MSL using results from the WRF simulation. The last red line is the average free-tropospheric temperature change (relative to $t = 0$) over CUR at 4000 m MSL using results from the WRF simulation.

(dominated by the northerly flow) impinging into NM occurs about 3 h before the frontal passage and the period of maximum precipitation.

APPENDIX B

Estimation of Climatological Mean Precipitation

To estimate the annual mean precipitation in the AFEX network over the NM, empirical corrections were applied to account for 1) the incomplete observing period within the year (e.g., May–September 2011) and 2) the general rainfall deficit (20%–30%) that affected south-central Chile since 2010. To this end, we made use of five conventional meteorological stations from DMC/DGA in the lowlands surrounding the NM that have a record length of at least 20 years and operated continuously during the AFEX period. These DMC/DGA

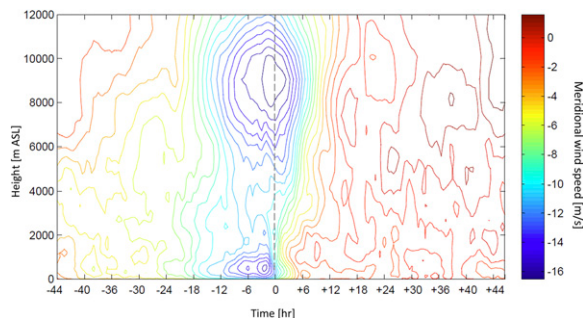


FIG. A3. Compositing analysis of the meridional wind speed during frontal passages over the NM. For each of the 26 frontal storms during the winter of 2011, we identified the time of maximum precipitation in station CUR at the mountains foothills, which is used as $t = 0$ for the compositing analysis (dashed black line). The composited meridional wind was constructed using the WRF results (inner domain) for a grid box just off the coast (about 50 km northwest of CUR).

stations are shown in Fig. 1b and their details are presented in Table B1.

Assuming a linear relationship with near-zero intercept between the annual accumulated precipitation in nearby locations, the long-term mean annual precipitation at an AFEX station [P_{AFEX}] can be estimated as:

$$[P_{\text{AFEX}}] = P_{\text{AFEX}}/P_{\text{CONV}} \times [P_{\text{CONV}}]$$

where [P_{CONV}] is the climatological annual precipitation in a conventional station, P_{AFEX} is the observed accumulation in the AFEX station, and P_{CONV} is the observed accumulation in the conventional station during the concurrent period. The linear relationship of the annual precipitation was verified when considering each pair of conventional stations, for which the correlation coefficient was always larger than 0.85. The full observing period was used for each AFEX stations, except for those located above 1000 m MSL (CAR, A3P, and PQE) since the snow that fell there in some winter storms was not properly measured in the nonheated HOBO rain gauges. For these three stations, the

TABLE B1. Name, location, and source of the conventional stations used to estimate the annual mean precipitation in the AFEX network (see details in appendix B).

Station name	Lat (S)	Lon (W)	Elev (m MSL)	Source
Curanilahue	37.29°	73.20°	140	DGA
Carampangue	37.23°	73.21°	13	DGA
Angol	37.48°	72.42°	79	DMC
Cañete	37.80°	73.39°	77	DMC
Puren	38.01°	73.20°	33	DGA

observing period only considered those storms when air temperature was always above 3°C to assure their pluvial character.

Thus, five estimates of the climatological annual accumulation were obtained for each AFEX station, enabling us to calculate a mean value and a standard deviation (level of uncertainty). The estimates were mostly consistent (within $\pm 15\%$ of the mean value), lending support to our method, the results of which are discussed in section 4a (Figs. 3,4).

REFERENCES

- Adam, J. C., and D. P. Lettenmaier, 2003: Adjustment of global gridded precipitation for systematic bias. *J. Geophys. Res.*, **108**, 4257, doi:10.1029/2002JD002499.
- , E. A. Clark, D. P. Lettenmaier, and E. F. Wood, 2006: Correction of global precipitation products for orographic effects. *J. Climate*, **19**, 15–38, doi:10.1175/JCLI3604.1.
- Alpert, P., and H. Shafir, 1989: Mesoscale distribution of orographic precipitation: Numerical study and comparison with precipitation derived from radar measurements. *J. Appl. Meteor.*, **28**, 1105–1117, doi:10.1175/1520-0450(1989)028<1105:MSDOOP>2.0.CO;2.
- Anders, A. M., G. H. Roe, D. R. Durran, and J. R. Minder, 2007: Small-scale spatial gradients in climatological precipitation on the Olympic Peninsula. *J. Hydrometeorol.*, **8**, 1068–1081, doi:10.1175/JHM610.1.
- , —, D. R. Montgomery, and B. Hallet, 2008: Influence of precipitation phase on the form of mountain ranges. *Geology*, **36**, 479–482, doi:10.1130/G24821A.1.
- Barros, A. P., and D. P. Lettenmaier, 1993: Dynamic modeling of the spatial distribution of precipitation in remote mountainous areas. *Mon. Wea. Rev.*, **121**, 1195–1214, doi:10.1175/1520-0493(1993)121<1195:DMOTSD>2.0.CO;2.
- , and —, 1994: Incorporation of an evaporative cooling scheme into a dynamic model of orographic precipitation. *Mon. Wea. Rev.*, **122**, 2777–2783, doi:10.1175/1520-0493(1994)122<2777:IOAECS>2.0.CO;2.
- Barstad, I., and R. B. Smith, 2005: Evaluation of an orographic precipitation model. *J. Hydrometeorol.*, **6**, 85–99, doi:10.1175/JHM-404.1.
- Basist, A., G. D. Bell, and V. Meentemeyer, 1994: Statistical relationships between topography and precipitation patterns. *J. Climate*, **7**, 1305–1315, doi:10.1175/1520-0442(1994)007<1305:SRBTAP>2.0.CO;2.
- Browning, K. A., 1986: Conceptual models of precipitation systems. *Wea. Forecasting*, **1**, 23–41, doi:10.1175/1520-0434(1986)001<0023:CMOPS>2.0.CO;2.
- , F. Hill, and C. Pardoe, 1974: Structure and mechanism of precipitation and the effect of orography in a wintertime warm sector. *Quart. J. Roy. Meteor. Soc.*, **100**, 309–330, doi:10.1002/qj.49710042505.
- , C. Pardoe, and F. Hill, 1975: The nature of orographic rain at wintertime cold fronts. *Quart. J. Roy. Meteor. Soc.*, **101**, 333–352, doi:10.1002/qj.49710142815.
- Colle, B. A., 2004: Sensitivity of orographic precipitation to changing ambient conditions and terrain geometries: An idealized modeling perspective. *J. Atmos. Sci.*, **61**, 588–606, doi:10.1175/1520-0469(2004)061<0588:SOOPTC>2.0.CO;2.
- , 2008: Two-dimensional idealized simulations of the impact of multiple windward ridges on orographic precipitation. *J. Atmos. Sci.*, **65**, 509–523, doi:10.1175/2007JAS2305.1.
- , and C. F. Mass, 1996: An observational and modeling study of the interaction of low-level southwesterly flow with the Olympic Mountains during COAST IOP 4. *Mon. Wea. Rev.*, **124**, 2152–2175, doi:10.1175/1520-0493(1996)124<2152:AOAMSO>2.0.CO;2.
- , —, and B. F. Smull, 1999: An observational and numerical study of a cold front interacting with the Olympic Mountains during COAST IOP5. *Mon. Wea. Rev.*, **127**, 1310–1334, doi:10.1175/1520-0493(1999)127<1310:AOANSO>2.0.CO;2.
- , B. F. Smull, and M.-J. Yang, 2002: Numerical simulations of a landfalling cold front observed during COAST: Rapid evolution and responsible mechanisms. *Mon. Wea. Rev.*, **130**, 1945–1966, doi:10.1175/1520-0493(2002)130<1945:NSOALC>2.0.CO;2.
- Cosma, S., E. Richard, and F. Miniscloux, 2002: The role of small-scale orographic features in the spatial distribution of precipitation. *Quart. J. Roy. Meteor. Soc.*, **128**, 75–92, doi:10.1256/00359000260498798.
- Daly, C., R. P. Neilson, and D. L. Phillips, 1994: A statistical-topographic model for mapping climatological precipitation over mountainous terrain. *J. Appl. Meteor.*, **33**, 140–158, doi:10.1175/1520-0450(1994)033<0140:ASTMFM>2.0.CO;2.
- , G. Taylor, and W. Gibson, 1997: The PRISM approach to mapping precipitation and temperature. Preprints, *10th Conf. on Applied Climatology*, Reno, NV, Amer. Meteor. Soc., 10–12.
- DGA, 1987: Balance Hídrico de Chile. Ministry of Public Works, Tech. Rep., 23 pp. [Available online at <http://sad.dga.cl/ipac20>.]
- Donoso, C., M. E. González, M. Cortés, C. González, P. Donoso, and M. Hernández, 2008: Poblaciones de araucaria enana (*Araucaria araucana*) en la Cordillera de Nahuelbuta, Chile. *Bosque (Valdivia)*, **29**, 170–175, doi:10.4067/S0717-92002008000200010.
- Dudhia, J., 1989: Numerical study of convection observed during the winter monsoon experiment using a mesoscale two-dimensional model. *J. Atmos. Sci.*, **46**, 3077–3107, doi:10.1175/1520-0469(1989)046<3077:NSOCOD>2.0.CO;2.
- Durran, D. R., and J. B. Klemp, 1982: The effects of moisture on trapped mountain lee waves. *J. Atmos. Sci.*, **39**, 2490–2506, doi:10.1175/1520-0469(1982)039<2490:TEOMOT>2.0.CO;2.
- Egger, J., and K. Hoinka, 1992: Fronts and orography. *Meteor. Atmos. Phys.*, **48**, 3–36, doi:10.1007/BF01029557.
- Endlicher, W., and R. Mäkel, 1985: Natural resources, land use and degradation in the coastal zone of Arauco and the Nahuelbuta Range, central Chile. *GeoJournal*, **11**, 43–60, doi:10.1007/BF00572938.
- Falvey, M., and R. Garreaud, 2007: Wintertime precipitation episodes in central Chile: Associated meteorological conditions and orographic influences. *J. Hydrometeorol.*, **8**, 171–193, doi:10.1175/JHM562.1.
- Frei, C., and C. Schär, 1998: A precipitation climatology of the Alps from high-resolution rain-gauge observations. *Int. J. Climatol.*, **18**, 873–900, doi:10.1002/(SICI)1097-0088(19980630)18:8<873::AID-JOC255>3.0.CO;2-9.
- Fuhrer, O., and C. Schär, 2005: Embedded cellular convection in moist flow past topography. *J. Atmos. Sci.*, **62**, 2810–2828, doi:10.1175/JAS3512.1.
- Garreaud, R., 2013: Warm winter storms in central Chile. *J. Hydrometeorol.*, **14**, 1515–1534, doi:10.1175/JHM-D-12-0135.1.
- Hevesi, J. A., J. D. Istok, and A. L. Flint, 1992: Precipitation estimation in mountainous terrain using multivariate geostatistics.

- Part I: Structural analysis. *J. Appl. Meteor.*, **31**, 661–676, doi:10.1175/1520-0450(1992)031<0661:PEIMTU>2.0.CO;2.
- Houze, R. A., Jr., and S. Medina, 2005: Turbulence as a mechanism for orographic precipitation enhancement. *J. Atmos. Sci.*, **62**, 3599–3623, doi:10.1175/JAS3555.1.
- , P. V. Hobbs, K. R. Biswas, and W. M. Davis, 1976: Mesoscale rainbands in extratropical cyclones. *Mon. Wea. Rev.*, **104**, 868–878, doi:10.1175/1520-0493(1976)104<0868:MRIEC>2.0.CO;2.
- Hughes, M., A. Hall, and R. G. Fovell, 2009: Blocking in areas of complex topography, and its influence on rainfall distribution. *J. Atmos. Sci.*, **66**, 508–518, doi:10.1175/2008JAS2689.1.
- Janjić, Z. I., 2000: Comments on “Development and evaluation of a convection scheme for use in climate models.” *J. Atmos. Sci.*, **57**, 3686–3686, doi:10.1175/1520-0469(2000)057<3686:CODAEO>2.0.CO;2.
- , 2002: Nonsingular implementation of the Mellor–Yamada level 2.5 scheme in the NCEP Meso model. NCEP Office Note 437, 61 pp. [Available online at <http://www.emc.ncep.noaa.gov/officenotes/newernotes/on437.pdf>.]
- Jiang, Q., 2003: Moist dynamics and orographic precipitation. *Tellus*, **55A**, 301–316, doi:10.1034/j.1600-0870.2003.00025.x.
- , and R. B. Smith, 2003: Cloud timescales and orographic precipitation. *J. Atmos. Sci.*, **60**, 1543–1559, doi:10.1175/2995.1.
- Kirshbaum, D. J., and D. R. Durran, 2004: Factors governing cellular convection in orographic precipitation. *J. Atmos. Sci.*, **61**, 682–698, doi:10.1175/1520-0469(2004)061<0682:FGCCIO>2.0.CO;2.
- , and —, 2005: Atmospheric factors governing banded orographic convection. *J. Atmos. Sci.*, **62**, 3758–3774, doi:10.1175/JAS3568.1.
- , G. H. Bryan, R. Rotunno, and D. R. Durran, 2007: The triggering of orographic rainbands by small-scale topography. *J. Atmos. Sci.*, **64**, 1530–1549, doi:10.1175/JAS3924.1.
- Kunz, M., and C. Kottmeier, 2006a: Orographic enhancement of precipitation over low mountain ranges. Part I: Model formulation and idealized simulations. *J. Appl. Meteor. Climatol.*, **45**, 1025–1040, doi:10.1175/JAM2389.1.
- , and —, 2006b: Orographic enhancement of precipitation over low mountain ranges. Part II: Simulations of heavy precipitation events over southwest Germany. *J. Appl. Meteor. Climatol.*, **45**, 1041–1055, doi:10.1175/JAM2390.1.
- Locatelli, J., J. Martin, and P. Hobbs, 1995: Development and propagation of precipitation cores on cold fronts. *Atmos. Res.*, **38**, 177–206, doi:10.1016/0169-8095(94)00093-S.
- Lundquist, J. D., J. R. Minder, P. J. Neiman, and E. Sukovich, 2010: Relationships between barrier jet heights, orographic precipitation gradients, and streamflow in the northern Sierra Nevada. *J. Hydrometeorol.*, **11**, 1141–1156, doi:10.1175/2010JHM1264.1.
- Matejka, T. J., R. A. Houze, and P. V. Hobbs, 1980: Microphysics and dynamics of clouds associated with mesoscale rainbands in extratropical cyclones. *Quart. J. Roy. Meteor. Soc.*, **106**, 29–56, doi:10.1002/qj.49710644704.
- Minder, J. R., D. R. Durran, G. H. Roe, and A. M. Anders, 2008: The climatology of small-scale orographic precipitation over the Olympic Mountains: Patterns and processes. *Quart. J. Roy. Meteor. Soc.*, **134**, 817–839, doi:10.1002/qj.258.
- Mlawer, E. J., S. J. Taubman, P. D. Brown, M. J. Iacono, and S. A. Clough, 1997: Radiative transfer for inhomogeneous atmosphere: RRTM, a validated correlated-*k* model for the longwave. *J. Geophys. Res.*, **102**, 16 663–16 682, doi:10.1029/97JD00237.
- Pleim, J. E., and A. Xiu, 2003: Development of a land surface model. Part II: Data assimilation. *J. Appl. Meteor.*, **42**, 1811–1822, doi:10.1175/1520-0450(2003)042<1811:DOALSM>2.0.CO;2.
- Prudhomme, C., and D. W. Reed, 1998: Relationships between extreme daily precipitation and topography in a mountainous region: A case study in Scotland. *Int. J. Climatol.*, **18**, 1439–1453, doi:10.1002/(SICI)1097-0088(19981115)18:13<1439::AID-JOC320>3.0.CO;2-7.
- , and —, 1999: Mapping extreme rainfall in a mountainous region using geostatistical techniques: A case study in Scotland. *Int. J. Climatol.*, **19**, 1337–1356, doi:10.1002/(SICI)1097-0088(199910)19:12<1337::AID-JOC421>3.0.CO;2-G.
- Reinecke, P. A., and D. R. Durran, 2008: Estimating topographic blocking using a Froude number when the static stability is nonuniform. *J. Atmos. Sci.*, **65**, 1035–1048, doi:10.1175/2007JAS2100.1.
- Roe, G. H., 2005: Orographic precipitation. *Annu. Rev. Earth Planet. Sci.*, **33**, 645–671, doi:10.1146/annurev.earth.33.092203.122541.
- , D. R. Montgomery, and B. Hallet, 2003: Orographic precipitation and the relief of mountain ranges. *J. Geophys. Res.*, **108**, 2315, doi:10.1029/2001JB001521.
- Sieck, L. C., S. J. Burges, and M. Steiner, 2007: Challenges in obtaining reliable measurements of point rainfall. *Water Resour. Res.*, **43**, W01420, doi:10.1029/2005WR004519.
- Sinclair, M. R., 1994: A diagnostic model for estimating orographic precipitation. *J. Appl. Meteor.*, **33**, 1163–1175, doi:10.1175/1520-0450(1994)033<1163:ADMFE0>2.0.CO;2.
- Skamarock, W. C., J. B. Klemp, J. Dudhia, D. O. Gill, D. M. Barker, W. Wang, and J. G. Powers, 2005: A description of the Advanced Research WRF version 2. NCAR Tech. Note NCAR/TN-468+STR, 88 pp., doi:10.5065/D6DZ069T.
- Smith, R. B., 1988: Linear theory of stratified flow past an isolated mountain in isosteric coordinates. *J. Atmos. Sci.*, **45**, 3889–3896, doi:10.1175/1520-0469(1988)045<3889:LTOSFP>2.0.CO;2.
- , 1989: Mountain-induced stagnation points in hydrostatic flow. *Tellus*, **41A**, 270–274, doi:10.1111/j.1600-0870.1989.tb00381.x.
- , 2003: A linear upslope-time-delay model for orographic precipitation. *J. Hydrol.*, **282**, 2–9, doi:10.1016/S0022-1694(03)00248-8.
- , 2006: Progress on the theory of orographic precipitation. *Spec. Pap. Geol. Soc. Amer.*, **398**, 1–16, doi:10.1130/2006.2398(01).
- , and I. Barstad, 2004: A linear theory of orographic precipitation. *J. Atmos. Sci.*, **61**, 1377–1391, doi:10.1175/1520-0469(2004)061<1377:ALTOOP>2.0.CO;2.
- , and J. P. Evans, 2007: Orographic precipitation and water vapor fractionation over the southern Andes. *J. Hydrometeorol.*, **8**, 3–19, doi:10.1175/JHM555.1.
- , I. Barstad, and L. Bonneau, 2005: Orographic precipitation and Oregon’s climate transition. *J. Atmos. Sci.*, **62**, 177–191, doi:10.1175/JAS-3376.1.
- Thompson, G., R. M. Rasmussen, and K. Manning, 2004: Explicit forecasts of winter precipitation using an improved bulk microphysics scheme. Part I: Description and sensitivity analysis. *Mon. Wea. Rev.*, **132**, 519–542, doi:10.1175/1520-0493(2004)132<0519:EFOWPU>2.0.CO;2.
- Viale, M., and R. Garreaud, 2015: Orographic effects of the subtropical and extratropical Andes on upwind precipitating clouds. *J. Geophys. Res. Atmos.*, **120**, 4962–4974, doi:10.1002/2014JD023014.
- Yang, D., B. E. Goodison, J. R. Metcalfe, V. S. Golubev, R. Bates, T. Pangburn, and C. L. Hanson, 1998: Accuracy of NWS 8” standard nonrecording precipitation gauge: Results and application of WMO intercomparison. *J. Atmos. Oceanic Technol.*, **15**, 54–68, doi:10.1175/1520-0426(1998)015<0054:AONSNP>2.0.CO;2.